Supplement of Atmos. Chem. Phys., 17, 13891–13901, 2017
https://doi.org/10.5194/acp-17-13891-2017-supplement

Supplement of

Insight into the in-cloud formation of oxalate based on in situ measurement by single particle mass spectrometry

Guohua Zhang et al.

Correspondence to: Xinhui Bi (bixh@gig.ac.cn)

Instrumentation

SPAMS

Individual particles are introduced into SPAMS through a critical orifice. They are focused and accelerated to specific velocities, which are determined by two continuous diode Nd:YAG laser beams (532 nm). Based on the measured velocities, a pulsed laser (266 nm) downstream is trigger to desorp/ionize the particles. The produced positive and negative molecular fragments are recorded. In summary, a velocity, a detection moment, and an ion mass spectrum are recorded for each ionized particle, while there is no mass spectrum for not ionized particles. The velocity could be converted to d_{va} based on a calibration using polystyrene latex spheres (PSL, Duke Scientific Corp., Palo Alto) with predefined sizes. The identified ion peaks have peak areas larger than 5 (arbitrary unit), whereas the noise level is lower than 1.

An discussion on the preferential association of oxalate within Fe-rich and Amine particles

As shown in Fig. 4, ~10% of oxalate was associated with Fe-rich particles, second only to the K-rich particles. Regarding that the Fe-rich particles only accounted for 2.5 ± 0.4% of all the detected particles (Lin et al., 2017), it might reflect that the Fe facilitated the formation of oxalate. Fenton reactions involving iron can produced more oxidants (e.g., •OH) (Nguyen et al., 2013; Herrmann et al., 2015), which is an important factor for the formation of oxalate (Ervens et al., 2014). While Sorooshian et al. (2013), Zhou et al. (2015), and Cheng et al. (2017) have suggested that oxalate can be significantly lost through the photolysis of iron-oxalato complexes. The difference between these observations and this study might be attributed to the different radiation. Our observation was conducted at a mountain site in winter, mostly covered with orographic cloud, resulted in very low visibility (< 500 m), and thus low radiation was expected during sampling. With sampling conducted on an aircraft, cloud water collected by Sorooshian et al. (2013) included the below and top of cloud water samples, and thus photolysis is expected. On the other hand, the highest fraction (> 30%) of oxalate was found to be internally mixed with metal-containing (e.g., iron, zinc, copper) particles in the Pearl River Delta region (Cheng et al., 2017). The internally mixed oxalate and iron could account for ~50% of iron particles at nighttime (Zhou et al., 2015). Additionally, oxalate was also found to be slightly enriched in amine-containing particles, which is most probably attributed to the enhanced partition of amine to wet aerosols (Rehbein et al., 2011; Zhang et al., 2012).

Table S1. Correlation analysis between the hourly detected number for species in cloud-free particles (N = 109) and ***cloud RES*** particles (N = 123). Most of the analysis shows significant correlation ($p < 0.001$) between the species, with the R^2 shown as follows. Results without significant correlation are marked with superscripts a and b.

	m/z -45	**m/z -59**	**m/z -71**	**m/z -73**	**m/z -89**	**K-rich**
m/z -45	1					
m/z -59	0.92/***0.93***	1				
m/z -71	0.77/***0.33***	0.92/***0.35***	1			
m/z -73	0.94/***0.81***	0.92/***0.86***	0.80/***0.20***	1		
m/z -89	0.22/***0.32***	0.38/***0.45***	0.46/***0.12***	0.33/***0.64***	1	
K-rich	0.52/**0.58**	0.33/**0.59**	0.21/***0*** [a]	0.57/***0.72***	0.05 [b] /**0.41**	1

[a] $p = 0.37$; [b] $p = 0.009$.

Table S2. Number fraction (%) of ion peaks for organic acids associated with all the detected particles and K-rich particles, respectively.

Ion peaks	All the detected particles (%)	K-rich particles (%)
m/z -45	12.4 ± 0.1	21.5 ± 0.3
m/z -59	8.6 ± 0.1	16.5 ± 0.3
m/z -71	2.8 ± 0.1	5.6 ± 0.1
m/z -73	12.6 ± 0.1	22.5 ± 0.3

Table S3. Number fraction (%) of the major OAs relative to all the detected particles, and visibility during each cloud event. Visibility was used here to indicate the cloud water content, since visibility is mainly controlled by the droplet number in cloud.

Ion peaks	**Cloud I**	**Cloud II**	**Cloud III**
m/z -45	16.5 ± 11.1	4.8 ± 1.2	8.6 ± 4.7
m/z -59	16.0 ± 9.6	3.9 ± 1.2	8.6 ± 5.5
m/z -71	8.7 ± 7.3	0.6 ± 0.4	4.0 ± 4.1
Visibility (km)	0.05 ± 0.03	0.31 ± 0.69	0.11 ± 0.17

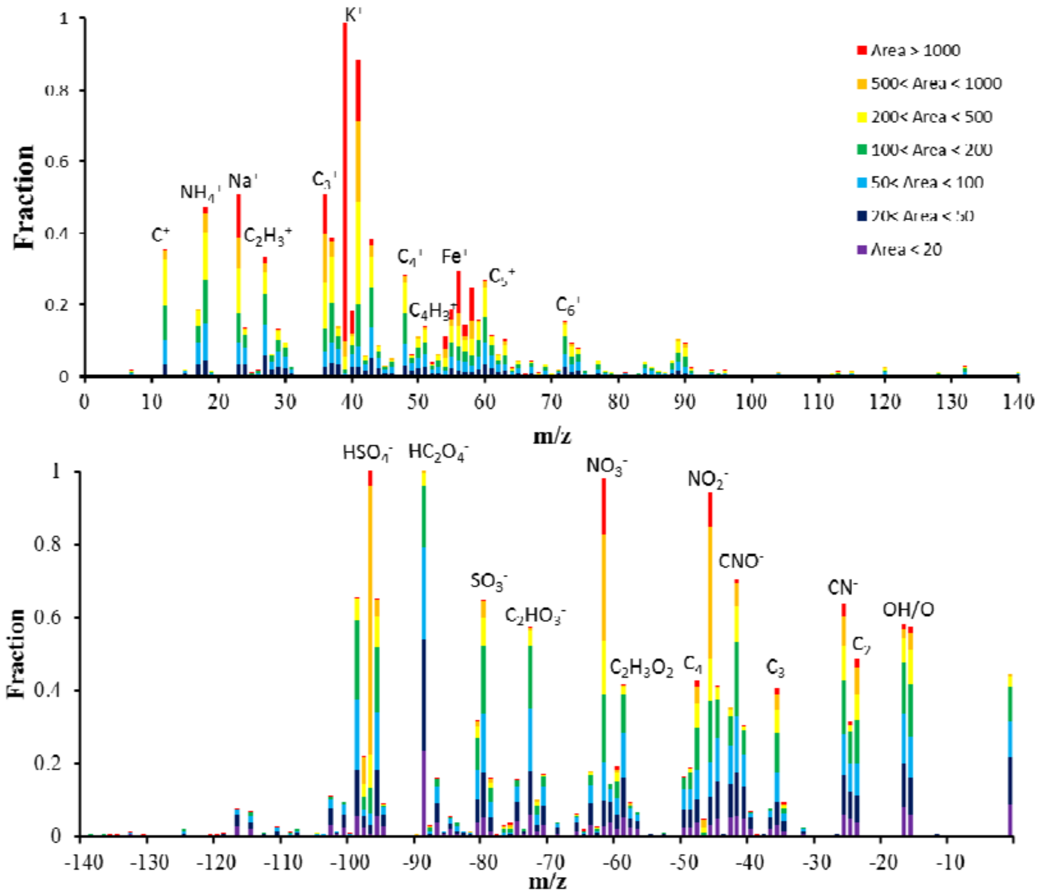

Figure S1. The number-based digitized mass spectrum of all the detected oxalate-containing particles. Compared with the number fraction of ammonium in Fig. 3, the result shows higher Nfs in oxalate-containing particles than ones in all particles, except m/z 18 (ammonium). As can be seen in Fig. 4, oxalate was dominantly distributed in K-rich particle type, which contained lower fraction of ammonium (~40%). However, as the dominant type in all the detected particles, EC type contained higher fraction (~80%) of ammonium. Therefore, the alkali nature (larger abundance of potassium, sodium) of the K-rich might explain the lower fraction of ammonium associated with the oxalate-containing particles.

(a)

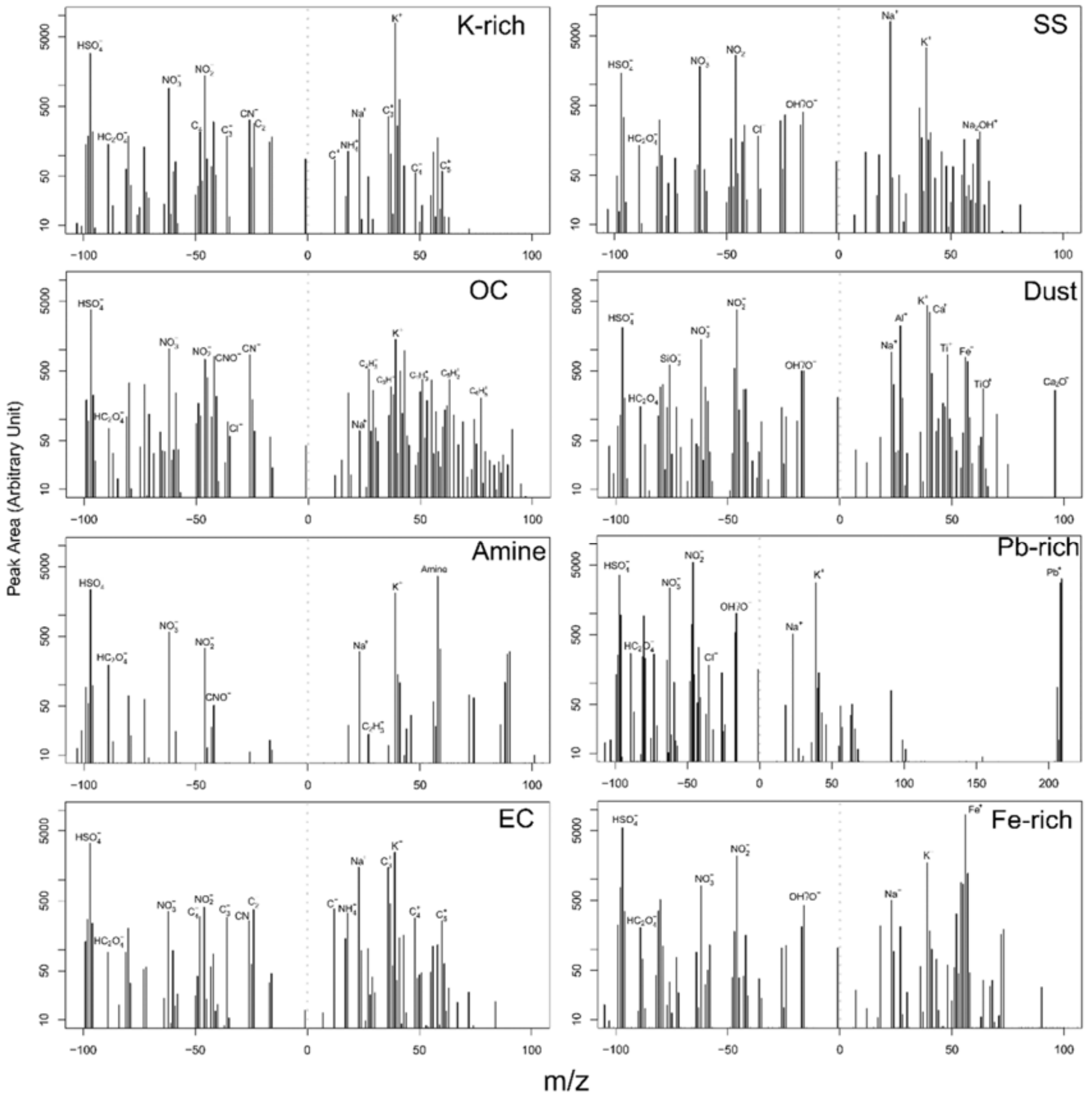
K-rich
SS
OC
Dust
Amine
Pb-rich
EC
Fe-rich
Peak Area (Arbitrary Unit)
m/z
HSO4-
HC2O4-
NO3-
NO2-
CN-
Na+
K+
Cl-
CNO-
Amine
Pb+
Fe+
Al+
Ca+
Ti+
OH-/O-
Na2OH+
Ca2O-
TiO+
SiO3-
NH4+
C2H3+

(b)

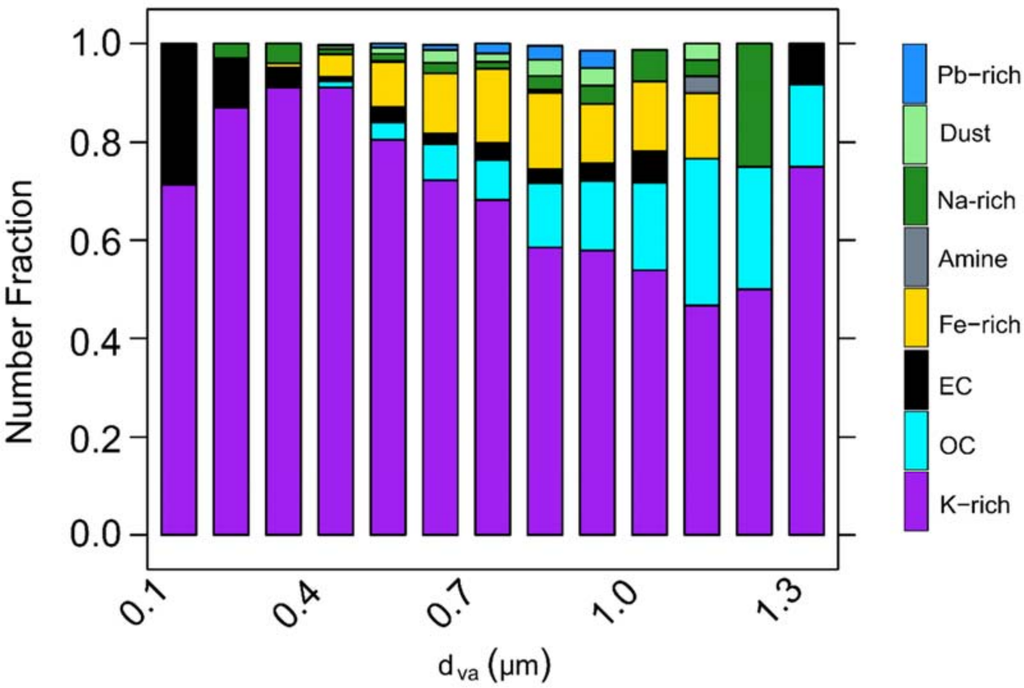

Figure S2. (a) Average mass spectra and (b) the size-resolved number fraction for each particle type of oxalate-containing particles. Representative ions peaks were labeled for each particle types. One may expect that oxalate at the largest d_{va} (1.3-1.4 μm) is associated with aged sea salt and/or mineral dust particles. However, our result shows that the aged biomass burning particles could contribute to the largest d_{va} (1.3-1.4 μm) mode of oxalate. However, it shouldn't be conclusive since only 12 particles were found at this size range.

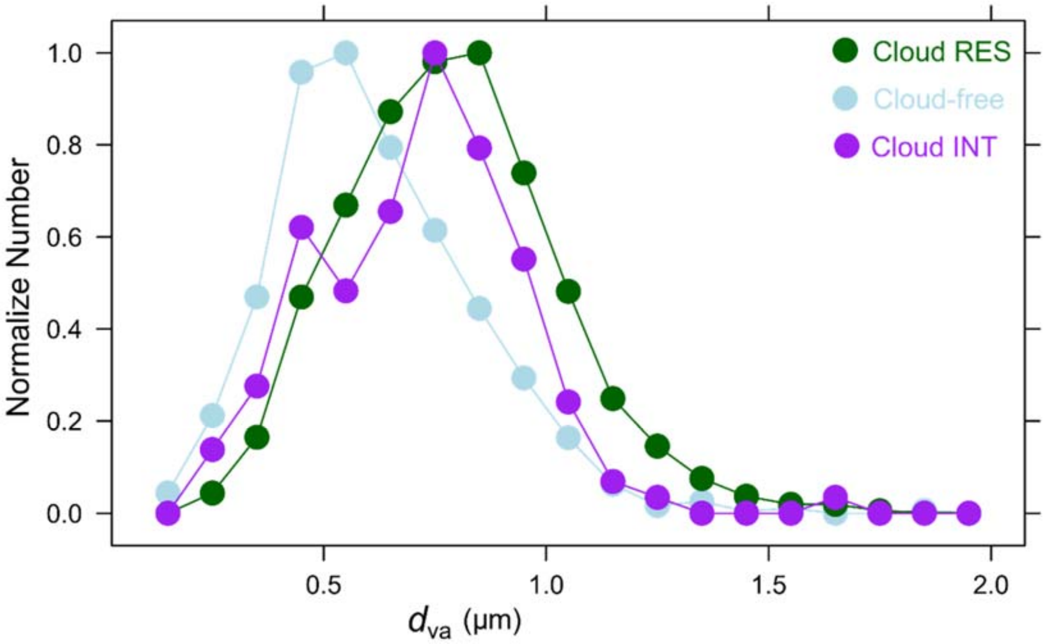

Figure S3. The normalized unscaled number size distribution of oxalate-containing particles in cloud-free, RES, and INT particles, respectively.

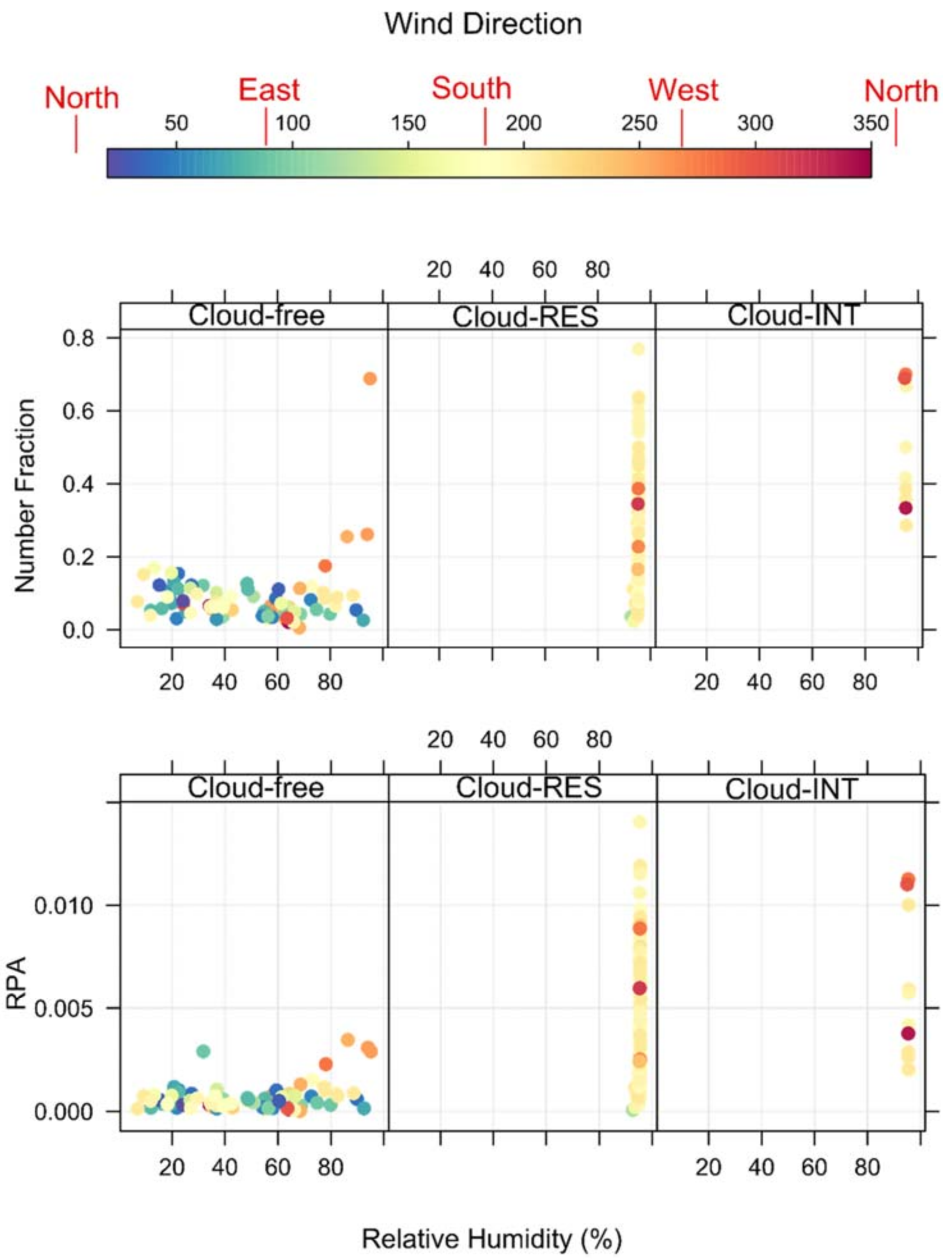

94

95 Figure S4. Scattering plots of (upper) the number fraction and (lower) the RPA of the

96 oxalate-containing particles versus relative humidity, separated for the cloud-free, cloud

97 RES, and cloud INT particles . The coloration indicates the wind direction.

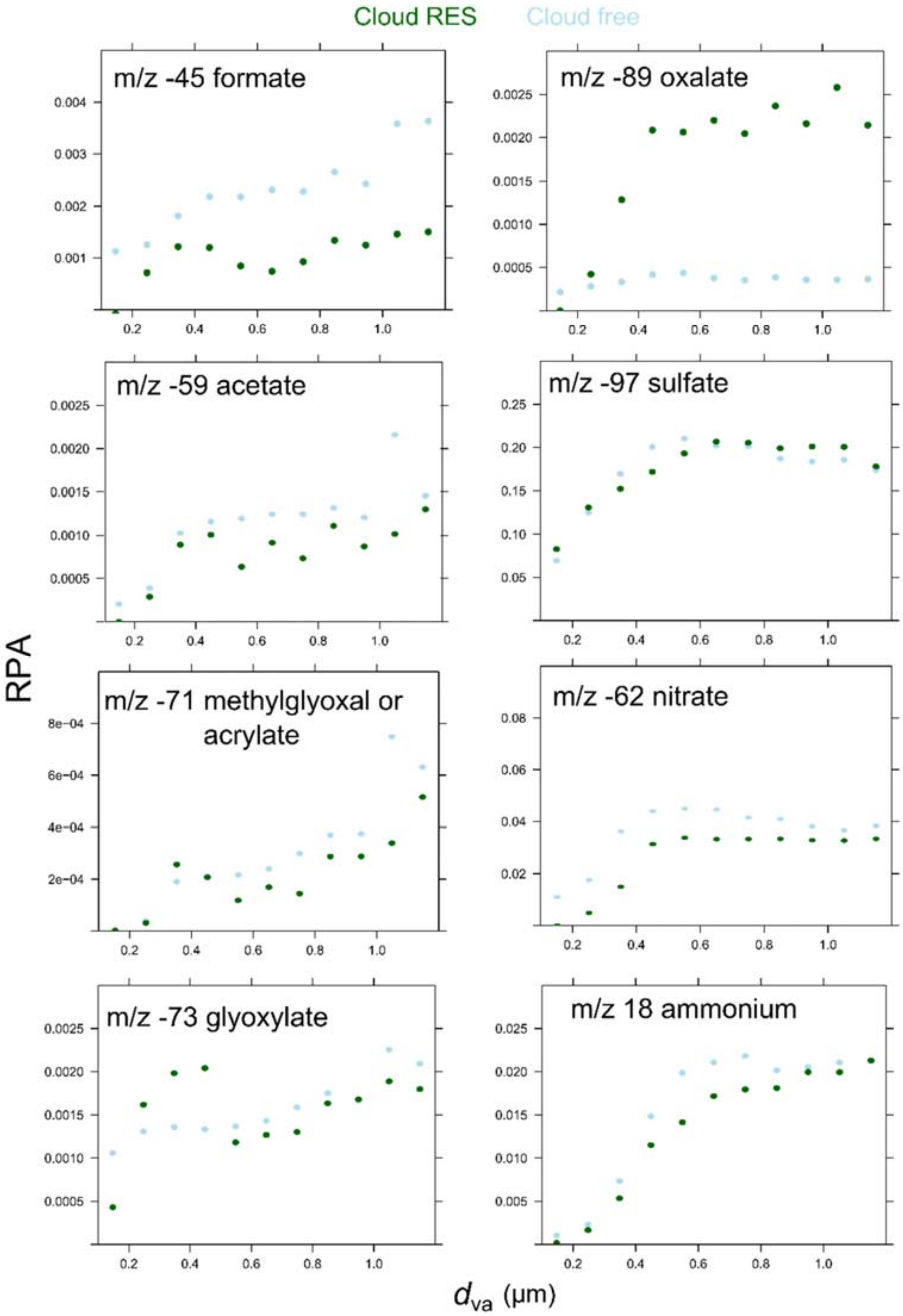

Figure S5. Size-resolved distribution of RPAs for each species in the cloud-free and RES particles.

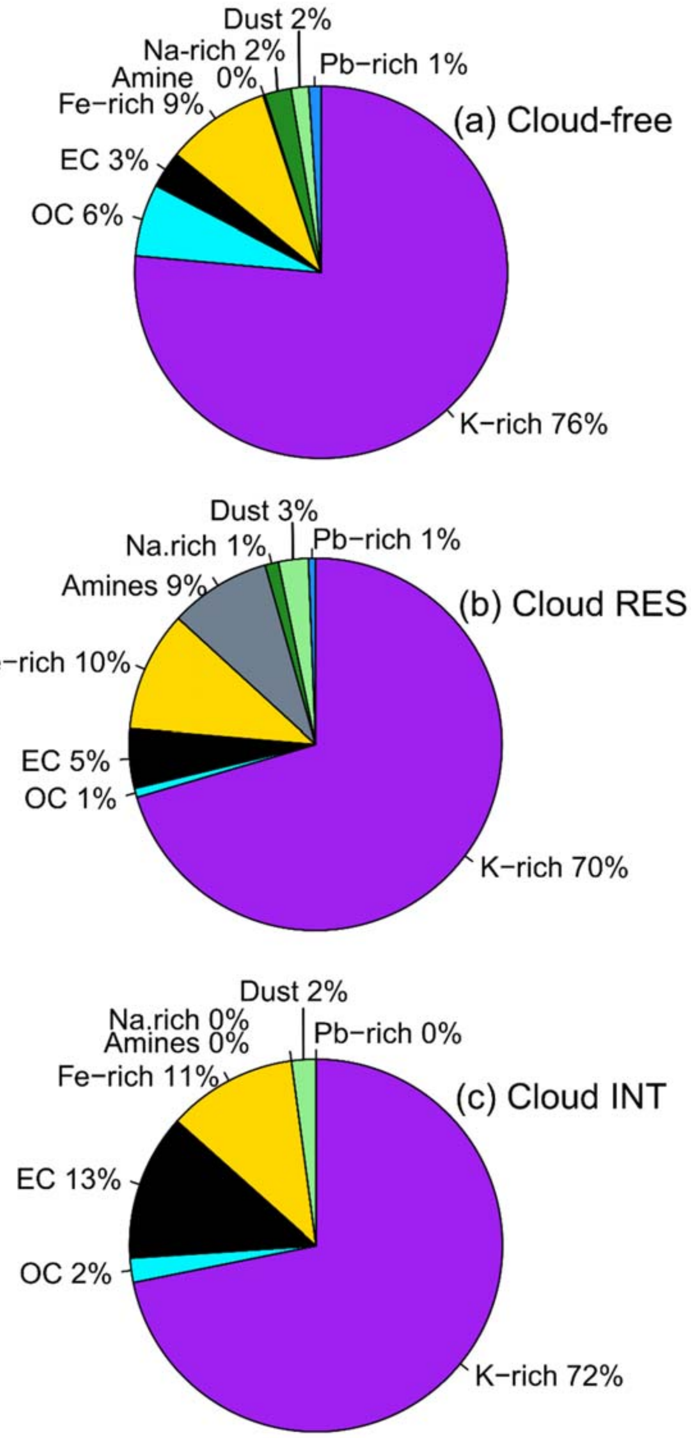

Figure S6. Number fraction of each oxalate-containing particle type for the (a) cloud-free, (b) cloud RES, and (c) cloud INT particles, respectively.

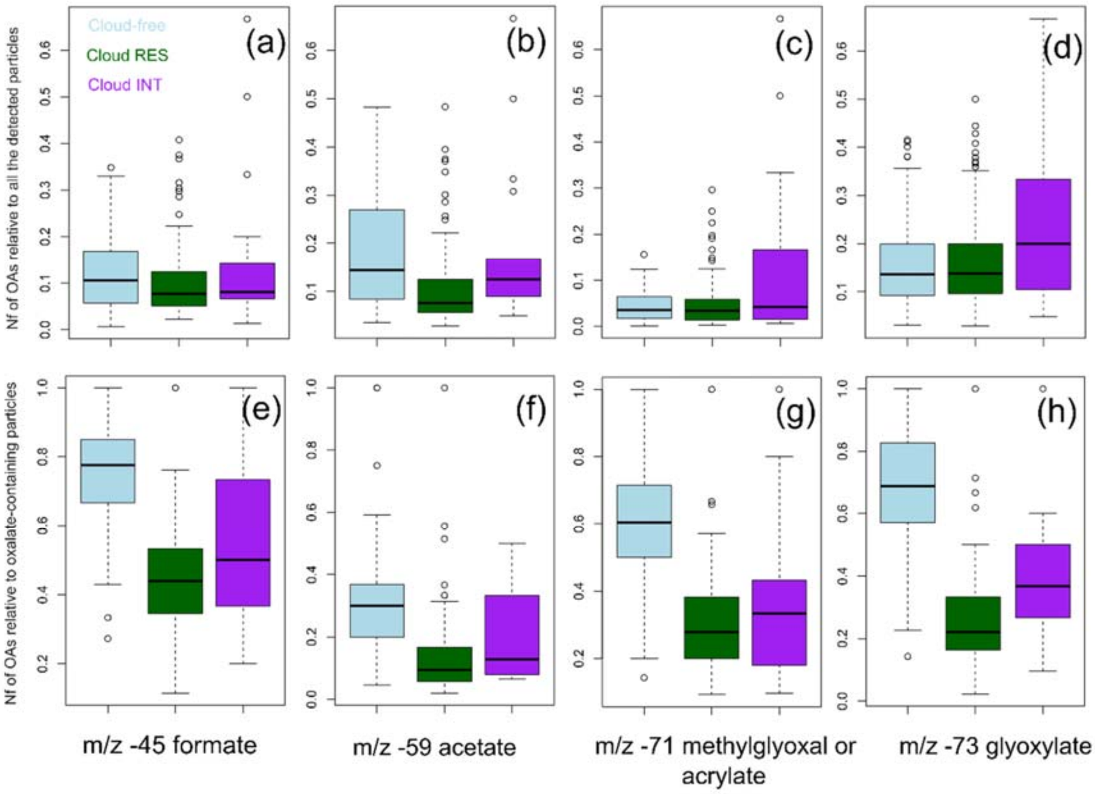

Figure S7. Box and whisker plot of the variations of number fractions for four OAs in (a-d) all the detected particles, and (e-h) oxalate-containing particles, separated for cloud-free, RES, and INT particles, respectively. In a box and whisker plot, the lower, median and upper line of the box denote the 25, 50, and 75 percentiles, respectively; the lower and upper edges of the whisker denote the 10 and 90 percentiles, respectively. Open circles shows the data not included between the whiskers, which is larger than 90 percentiles or lower than 10 percentiles of the data set.

References

Cheng, C., Li, M., Chan, C. K., Tong, H., Chen, C., Chen, D., Wu, D., Li, L., Wu, C., Cheng, P., Gao, W., Huang, Z., Li, X., Zhang, Z., Fu, Z., Bi, Y., and Zhou, Z.: Mixing state of oxalic acid containing particles in the rural area of Pearl River Delta, China: implications for the formation mechanism of oxalic acid, Atmos. Chem. Phys., 17, 9519-9533, doi:10.5194/acp-17-9519-2017, 2017.

Ervens, B., Sorooshian, A., Lim, Y. B., and Turpin, B. J.: Key parameters controlling OH-initiated formation of secondary organic aerosol in the aqueous phase (aqSOA), J. Geophys. Res.-Atmos., 119, 3997-4016, doi:10.1002/2013JD021021, 2014.

Herrmann, H., Schaefer, T., Tilgner, A., Styler, S. A., Weller, C., Teich, M., and Otto, T.: Tropospheric Aqueous-Phase Chemistry: Kinetics, Mechanisms, and Its Coupling to a Changing Gas Phase, Chem. Rev., 115, 4259-4334, doi:10.1021/cr500447k, 2015.

Nguyen, T. B., Coggon, M. M., Flagan, R. C., and Seinfeld, J. H.: Reactive Uptake and Photo-Fenton Oxidation of Glycolaldehyde in Aerosol Liquid Water, Environ. Sci. Technol., 47, 4307-4316, doi:10.1021/es400538j, 2013.

Rehbein, P. J. G., Jeong, C. H., McGuire, M. L., Yao, X. H., Corbin, J. C., and Evans, G. J.: Cloud and Fog Processing Enhanced Gas-to-Particle Partitioning of Trimethylamine, Environ. Sci. Technol., 45, 4346-4352, doi:10.1021/es1042113, 2011.

Sorooshian, A., Wang, Z., Coggon, M. M., Jonsson, H. H., and Ervens, B.: Observations of Sharp Oxalate Reductions in Stratocumulus Clouds at Variable Altitudes: Organic Acid and Metal Measurements During the 2011 E-PEACE Campaign, Environ. Sci. Technol., 47, 7747-7756, doi:10.1021/es4012383, 2013.

Zhang, G. H., Bi, X. H., Chan, L. Y., Li, L., Wang, X. M., Feng, J. L., Sheng, G. Y., Fu, J. M., Li, M., and Zhou, Z.: Enhanced trimethylamine-containing particles during fog events detected by single particle aerosol mass spectrometry in urban Guangzhou, China, Atmos. Environ., 55, 121-126, doi:10.1016/j.atmosenv.2012.03.038, 2012.

Zhou, Y., Huang, X. H., Bian, Q., Griffith, S. M., Louie, P. K. K., and Yu, J. Z.: Sources and atmospheric processes impacting oxalate at a suburban coastal site in Hong Kong: Insights inferred from 1 year hourly measurements, J. Geophys. Res.-Atmos., 120, 9772-9788, doi:10.1002/2015jd023531, 2015.